This is the accepted manuscript made available via CHORUS. The article has been published as:

Magnetotransport properties of MoP_{2}

Aifeng Wang (□□□), D. Graf, Aaron Stein, Yu Liu (□□), Weiguo Yin (□□□), and C. Petrovic

Phys. Rev. B **96**, 195107 — Published 2 November 2017

DOI: 10.1103/PhysRevB.96.195107

Magnetotransport properties of MoP_2

Aifeng Wang (王爱峰),[1] D. Graf,[2] Aaron Stein,[3] Yu Liu (刘育),[1] Weiguo Yin (尹卫国)[1] and C. Petrovic[1]
[1] *Condensed Matter Physics and Materials Science Department, Brookhaven National Laboratory, Upton, New York 11973, USA*
[2] *National High Magnetic Field Laboratory, Florida State University, Tallahassee, Florida 32306-4005, USA*
[2] *Center for Functional Nanomaterials, Brookhaven National Laboratory, Upton, New York 11973-5000, USA*
(Dated: October 17, 2017)

We report magnetotransport and de Haas-van Alphen (dHvA) effect studies on MoP_2 single crystals, predicted to be type-II Weyl semimetal with four pairs of robust Weyl points located below the Fermi level and long Fermi arcs. The temperature dependence of resistivity shows a peak before saturation, which does not move with magnetic field. Large nonsaturating magnetoresistance (MR) was observed, and the field dependence of MR exhibits a crossover from semicalssical weak-field B^2 dependence to the high-field linear-field dependence, indicating the presence of Dirac linear energy dispersion. In addition, systematic violation of Kohler's rule was observed, consistent with multiband electronic transport. Strong spin-orbit coupling (SOC) splitting has an effect on dHvA measurements whereas the angular-dependent dHvA orbit frequencies agree well with the calculated Fermi surface. The cyclotron effective mass $\sim 1.6m_e$ indicates the bands might be trivial, possibly since the Weyl points are located below the Fermi level.

PACS numbers: 72.20.My, 72.80.Jc, 75.47.Np

I. INTRODUCTION

Weyl fermions in condensed-matter systems have attracted considerable interest and are intensively studied.[1–3] Two types of Weyl fermions were found in solid materials. Type-I Weyl semimetal (WSM) has an ideal Weyl cone in the electronic structure and a closed point-like Fermi surface with Lorentz symmetry, while the type-II WSM has a strongly tilted Weyl cone where the Fermi surface consists of an electron and a hole pocket that touch at the Weyl node in a topologically protected manner.[4,5] Thus, Type-II WSM could have some exotic properties, such as anisotropic chiral anomaly, anomalous Hall effect, and Klein tunneling.[4,6,7]

The two originally proposed type-II WSM materials are WTe_2 and $MoTe_2$.[4,8] However, the arrangement of Weyl points (WPs) is very sensitive to crystal structure. The proximity of WPs with opposite Chern numbers, and the WPs location above the Fermi level makes WPs in WTe_2 and $MoTe_2$ unstable and difficult to probe.[8] WSM can be obtained by either breaking time-reversal symmetry or space-inversion symmetry in a Dirac semimetal.[9] MoP_2, with a similar chemical formula and nonsymmorphic space group $Cmc2_1$ (36), serves as a good candidate for a type-II WSM. Recently, MoP_2 was predicted to be a type-II WSM with stable WPs located below the Fermi level and long Fermi arcs, which can be studied by angle-resolved photoemission spectroscopy (ARPES) measurements.[10]

In this paper, we have successfully grown single crystals of MoP_2, and performed magnetotransport and de Haas-van Alphen (dHvA) measurements. We found that a peak appears in the temperature dependence of resistivity at 45 K that does not change in magnetic fields up to 9T. With increasing magnetic field, magnetoresistance (MR) exhibits a crossover from semiclassical B^2 dependence to the linear-field dependence at critical field B^*; the B^* can be described by quadratic behavior for quantum limit with linear energy dispersion. Moreover, a systematic violation of Kohler's rule was observed. The effective mass detected by dHvA is $m \cong 1.6m_e$, indicating that the band probed by dHvA is relatively trivial, possibly since WPs are located below the Fermi level. Though the crystal structure of MoP_2 is three-dimensional (3D) without obvious stacks of layered two-dimensional building blocks, angular-dependent dHvA measurement reveal quasi-2D Fermi surface in MoP_2 whereas the results of the dHvA measurement agree well with the calculated Fermi surface.

II. EXPERIMENTAL DETAILS

Single crystals of MoP_2 were grown by the chemical iodine vapor transport method. Polycrystal of MoP_2 was synthesized by heating stoichiometric amounts of Mo and P powders at 500 °C for 24 h, and then 750 °C for 48 h. 1 g MoP_2 polycrystal was mixed with I_2 (15 mg/ml), and then sealed in an evacuated quartz tube. Single crystals were grown in the temperature gradient 1050 °C (source) to 950 °C (sink) for two weeks. Small needle-like single crystal with typical size 200 μm × 50 μm × 20 μm were obtained. Single crystal x-ray diffraction (XRD) measurements were performed using a Bruker Apex II single crystal x-ray diffractometer with Mo K_α radiation (λ = 0.071073 nm) at room temperature. The elemental analysis was performed using an energy-dispersive x-ray spectroscopy (EDX) in a JEOL LSM 6500 scanning electron microscope. Electrical transport were performed using Quantum Design PPMS-9. The dHvA effect at high magnetic field up to 18 T was measured at the National High Magnetic Field Laboratory (NHMFL) in Tallahassee.

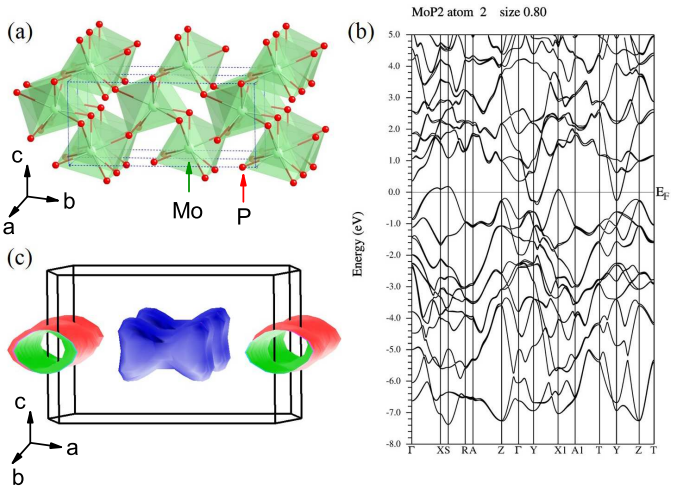

FIG. 1. (Color online). (a) Crystal structure of MoP_2. (b) The band structure for MoP_2. (c) Fermi surface of MoP_2, a pair of bow-tie-like Fermi pockets are located around Y point in the BZ, and a pair of spaghetti-like hole Fermi pockets are located at X point of BZ.

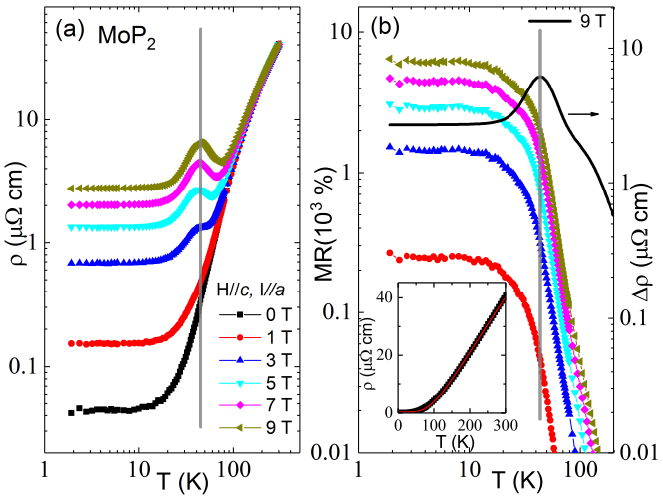

FIG. 2. (Color online). (a) Temperature dependence of resistivity in different magnetic fields plotted on a log-log scale, the magnetic field is applied along c axis, and electrical current is along a axis. The grey vertical line is a guide to eye. (b) The temperature dependence of the MR = (ρ(B) - ρ(0T))/ρ(0T) $\times$ 100% at different fields (left), and the $\Delta\rho$ = ρ(9T) - ρ(0T) (right). (a) and (b) use the same legend. Inset shows ρ(0T) fitted with Bloch-Grüneisen model.

Resistivity was measured using a standard four contact configuration. For first-principles band structure calculations, we applied the WIEN2K[11] implementation of the full potential linearized augmented plane wave method in the generalized gradient approximation[12] of density-functional theory with spin-orbit coupling treated in a second variational method. The basis size was determined by $R_{\rm mt}K_{\rm max} = 7$ and the Brillouin zone was sampled with a regular $19\times19\times11$ mesh containing 600 irreducible k points to achieve energy convergence of 1 meV. Fermi surface was plotted in a 10,000 k-point mesh.

III. RESULTS AND DISCUSSIONS

The crystal structure of MoP_2 is shown in Fig. 1(a), each Mo atom is surrounded by seven P atoms in nearly octahedral coordination. MoP_2 with space group $Cmc2_1$ (36) is composed by the stacking of the incomplete octahedra in three directions, having a mirror plane perpendicular to a axis, a c-glide plane perpendicular to b axis, and a two fold screw axis parallel to c axis. Crystal structure without space-inversion symmetry makes MoP_2 a good candidate for Weyl semimetal. The lattice parameters a = 3.13(1) Å, b = 11.12(1) Å, and c = 4.94(1) Å determined by single crystal XRD agree well with previous report.[13] The average Mo: P atomic ratio determined by EDX is close to 1 : 2, consistent with the composition of MoP_2. The calculated band structure and Fermi surface of MoP_2 are shown in Figs. 1(b) and 1(c), respectively. Band splitting induced by spin-orbit coupling was observed. There is a pair of bow-tie-like closed electron pockets at Y-point of the Brillouin zone (BZ), and spaghetti-like open hole Fermi surfaces at X-point of BZ, which are extended along the b axis, flat along the c axis, and warped along the a axis. The band structure and Fermi surface are similar to WP_2.[10,14,15]

The temperature dependence of resistivity in different magnetic fields were measured with B parallel to the crystallographic c axis and current parallel to the a axis, as shown in Fig. 2(a). $\rho(0T)$ shows a metallic behavior with ρ(2K) = 0.042 $\mu\Omega$cm and RRR = 965, indicating very high quality of our single crystals. $\rho(0T)$ curve can be well fitted by the Bloch-Grüneisen (BG) model:[16]

$$\rho(T) = \rho_0 + C(\frac{T}{\Theta_D})^5 \int_0^{\frac{\Theta_D}{T}} \frac{x^5}{(e^x-1)(1-e^{-x})}dx$$

where ρ_0 is the residual resistivity and Θ_D is the Debye temperature. The fitting gives Θ_D = 591 K, similar to that of WP_2.[17] The good BG model fit suggests that the phonon scattering dominates in the absence of magnetic field. As shown in Fig. 2(a), a magnetic field-induced resistivity upturn was observed at low temperature, in contrast to other semimetals such as TaAs, WTe_2, and LaSb.[2,19,20] The resistivity diminishes with further decrease in temperature and saturates below $\sim$ 14 K. Peak temperature position in $\rho(T)$ at 45 K does not move with field and is shown by the vertical line in Fig. 2(a). We note that a weak peak was also observed in WP_2.[14] Even though the peak can be observed in $\Delta\rho$, the MR monotonously increases with decreasing temperature and saturates at $\sim$ 14 K, as shown in Fig. 2(b). In order to understand the peak effect we measured magnetic field dependence of MR at different temperatures.

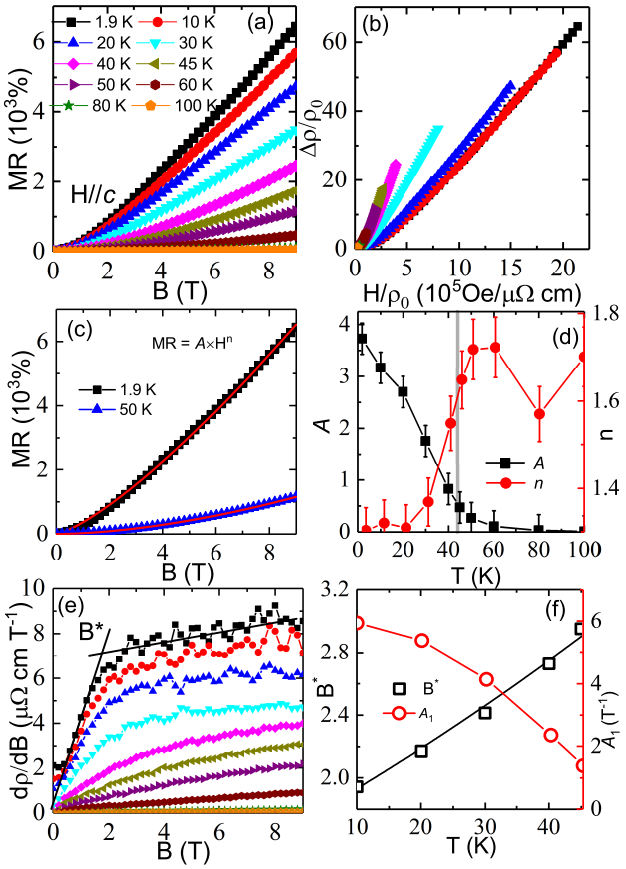

FIG. 3. (Color online). The MR vs magnetic field at different temperatures for MoP_2 with $H//b$. (b) A Kohler plot for MoP_2. (c) Typical magnetic field dependence of MR curves, the solid lines are fits using MR = $A\times H^n$. (d) Temperature dependence of A (left) and n (right) in MR = $A\times H^n$. (e) The field derivative of MR (d(MR)/dB at different temperatures, solid lines show the criterion used to determine the critical field B^*. (f) Temperature dependence of the critical field B^* (left); the black solid line is the fitting of B^* by $B^* = \frac{1}{2e\hbar v_F^2}(E_F + k_BT)^2$. The red circle corresponds to high-field MR linear coefficient A_1.

A square to linear transition of field dependent MR was observed, and the MR can reach as high as 6.45×10^3 % at 1.9 K and 9 T [Fig. 3(a)]. This is similar to Ta_3S_2,[18] one or two order of magnitude smaller when compared to WTe_2 and LaSb.[19,20] According to semiclassical transport theory, if there is a single type of charge carrier and scatting in a metal, Kohler's rule states that the relative change in resistivity $\Delta\rho/\rho_0$ in a magnetic field H is a universal function of H/ρ_0, where ρ_0 is the zero-field resistivity at certain temperature.[21] As shown in Fig. 3(b), while the data below 45 K deviate from Kohler's rule, the data above 45 K still fall on same curve, suggesting that the transport above 45 K is dominated by a single scattering process. Multiple reasons can lead to the breakdown of Kohler's law, for example a multiband effect with different scattering times. We fit the MR with a simple power law MR = $A \times H^n$, the typical data is shown in fig. 3(c). The MR above 45 K can be well fitted in the whole range, but there are some deviations in the low field range of the data below 45 K. The obtained parameters are shown in Fig. 3(d), A monotonously decreases with temperature increase and n increases with increasing temperature and saturates at ~ 1.7. n should be 2 in a conventional metal, while linear MR is often observed in Dirac semimetals. One of the possible explanations for the temperature dependence of n is that the Dirac band plays a more important role as the temperature is lowered. Assuming similarity with WP_2, the carrier density of MoP_2 might be relatively high.[17] Due to the small effective mass and long mean free path, Dirac fermions are likely to show their footprint in the exponent of field-dependent MR reduced from the square.

A peak was observed in temperature dependence of $\Delta\rho$ = [ρ(T,H)-ρ(T,0)] in pure metals such as copper, aluminum and indium, which can be explained by the two band model.[22–24] This mechanism is not likely to cause the peak observed in MoP_2 since the peak temperature in pure metals increases with increasing field, in contrast to nearly magnetic field-independent peak in MoP_2. The peak also cannot be explained by the graphite-like superconducting correlations in the quantum limit since it also increases with increasing field.[25] On the other hand, systematic evolution of A and n [Fig. 3(d)] suggests that the peak might be the result of interplay of the temperature dependent weight of linear MR and square MR, i.e. Dirac and normal Fermions.

In order to characterize the crossover behavior from weak-field B^2 dependence to the high-field linear dependence, we present the field derivative of the MR, dMR/dB, in Fig. 3(e). Linear field dependences for dMR/dB in low fields agree with the semiclassical MR $\sim A_2B^2$. With field increasing, dMR/dB reduces from linear behavior to a weak field dependence saturating behavior above a characteristic field B^*, indicating that MR is dominated by a linear field dependence plus a small quadratic term [$\Delta\rho/\rho = A_1B + o(B^2)$] at high field region.[26,27] Since the splitting between the lowest and first Landau level (LL) for Dirac state is described as $\Delta_{LL} = \pm v_F\sqrt{2e\hbar B}$, where $\Delta_{LL} = \frac{e\hbar B}{m^*}$ for a conventional parabolic band, quantum limit is easily reached for Dirac band.[26] As shown in Fig. 3(f), B^* can be described by critical field for quantum limit at a specific temperature $B^* = \frac{1}{2e\hbar v_F^2}(E_F + k_BT)^2$,[28] suggesting the linear MR likely originates from the Dirac states.

Figures 4(a) and 4(b) show the MR with field tilted from c axis to b axis. The MR at 2 K and 18 T is 1.6×10^4% along the c axis, and 2.5×10^4% along the b axis. Angular dependence of the MR with magnetic filed perpendicular to the electric current is shown in Fig. 4(c). In contrast to WP_2 where angular dependence of MR shows 2D behavior,[14,15,17] MoP_2 shows four fold symmetry. The different bc plane symmetry and similarity of Fermi surfaces of MoP_2 and WP_2 indicate that the transport properties are sensitive to the fine details of Fermi surface and/or the spin-orbital coupling. We also fit the

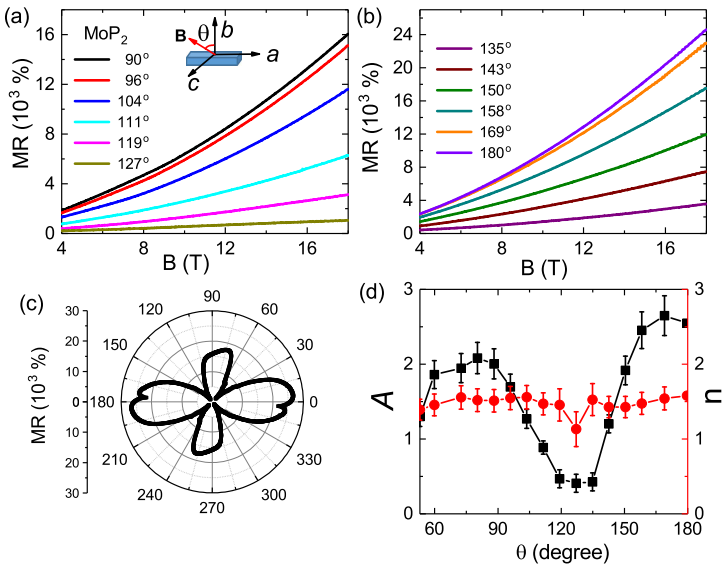

FIG. 4. (Color online). (a) and (b) Magnetic field dependence of MR with field at different angles in bc plane. The current is along a axis and always perpendicular to the field. (c) Polar plot of the angular dependence of the MR with the field rotated in bc plane at 2 K and 18 T. (d) Temperature dependence of A (left) and n (right) in MR = $A \times H^n$.

MR at different angles with power law MR = $A \times H^n$, as shown in Fig.4(d). Whereas A shows similar angular dependence as MR amplitude does, n is nearly constant with angle.

Quantum oscillation is a powerful tool in investigating Weyl/Dirac materials. We measured de Haas-van Alphen (dHvA) oscillations in MoP_2 at different temperatures, as shown in Fig.5(a). Beat patterns were observed, indicating that multiple frequencies contribute to the oscillations. The corresponding fast Fourier transform (FFT) spectra is shown in Fig. 5(b), similar to that of WP_2. Three frequencies are observed: 1261 T, 1371 T, and 1469 T. According to Onsager relation, $F = (\Phi_0/2\pi^2)A_F$, where Φ_0 is the flux quantum and A_F is the orthogonal cross-sectional area of the Fermi surface, the Fermi surface is estimated to be 12 nm^{-2}, 13 nm^{-2}, and 14 nm^{-2}. This corresponds to 4.7%, 5.1%, and 5.5% of the total area of the Brillouin zone in the ac plane. The oscillations dampen quickly with temperature and disappear above 4.2 K, indicating a heavy cyclotron mass in MoP_2. The temperature dependence of amplitude of the oscillations is fitted using the Lifshitz-Kosevich formula,[29] $A \sim [\alpha m^*(\mathrm{T/B})/\sinh(\alpha\, m^*\mathrm{T/B})]$ where $\alpha = 2\pi^2 k_B/e\hbar \approx 14.69$ T/K, $m^* = m/m_e$ is the cyclotron mass ratio (m_e is the mass of free electron), as exhibited in Fig. 5(c). The fitting gives $m^* \cong 1.6$, similar to that in WP_2, possibly due to electron-phonon many body interactions.[14] The effective cyclotron mass suggests that the band detected by the dHvA effect might be trivial, in agreement with location of the Weyl points below the Fermi level.[10] The trivial Fermi surfaces are not consistent with the Dirac

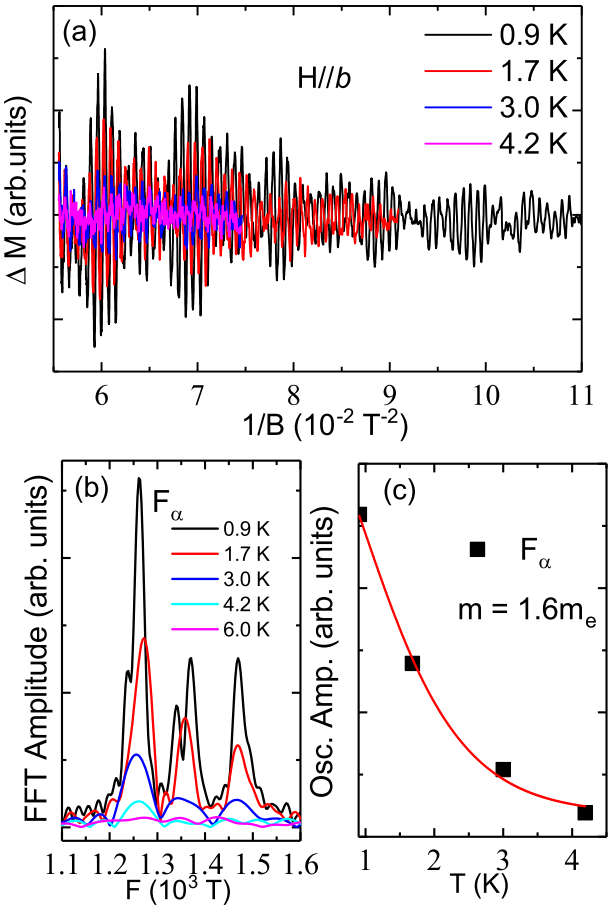

FIG. 5. (Color online). (a) dHvA oscillatory components at different temperatures obtained by subtracting smooth background. (b) FFT spectra for the dHvA oscillations in (a). (c) Temperature dependence of the oscillating amplitude at F_α = 1261 T, solid line is fitted using Lifshitz-Kosevich formula.

states indicated by linear MR. A possible explanation is that the Dirac state usually leads to a small Fermi surface and therefore might not be easily detected by dHvA measurement. This is similar to the case in MoP, where a triply degenerate point with Dirac-like dispersion well below Fermi level has been discovered.[30]

Angular-dependent dHvA oscillations provide further insights into Fermi surface properties. The FFT spectra of dHvA oscillations are shown in Fig. 6(a,b) for magnetic field rotated in the bc and ab planes, respectively. The positions of the FFT peaks are summarized in Fig. 6(c) and Fig. 6(d). The FFT peaks can be generally divided into two groups, one group around 1200 T, and another group around 3000 T. According to the calculated Fermi surface, as shown in Fig.1(c), lower frequencies around 1200 T should arise from the oscillation of spaghetti-like open hole Fermi surface, while higher frequencies around 3000 T are due to the oscillation of bow-tie-like closed electron Fermi surface. Split peaks and small peaks around the main peaks might

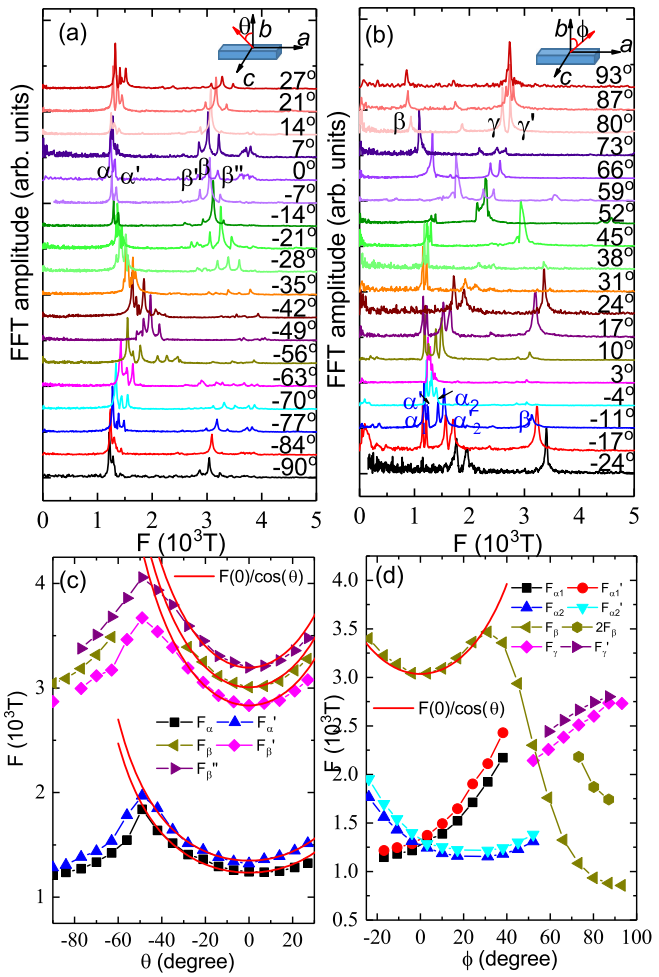

FIG. 6. (Color online). FFT spectra of dHvA oscillaiton with field rotated in the *bc* plane (a) and in the *ab* plane (b); the spectra are nomalized and shifted vertically for clearity. (c,d) Angular dependence of the oscillation frequency corresponding to the oscillation in (a) and (b), respectively. Red solid lines are fits with 2D model $F(0)/\cos(\theta)$.

be due to strong spin-orbit coupling and warped Fermi surface.[14] Even though the crystal structure is three-dimensional and quite different from the quasi-2D structure of $SrMnBi_2$ with square Bi layers,[26] all peaks show quasi-2D angle dependence $[F(0)/cos(\theta)]$ at low angles around H//*b*, indicating quasi-2D FS in MoP_2 [Fig. 6(c)]. The peaks show symmetry behavior at $\sim 50^o$, indicating possible four fold symmetry in *bc* plane, consistent with the four fold symmetry of MR in *bc* plane. When the magnetic field is rotated in the *ab* plane, peaks corresponding to hole pocket show behavior of two elliptical FS enlongated $\sim 25^o$ away from the *b* axis. This is consistent with the calculated spaghetti-like hole pocket.[10,14] As shown in Fig. 1(c), the spaghetti-like hole pocket is flat along the *ab* plane, indicating quasi-2D like behavior with magnetic field rotated in *bc* plane, while it is rather warped in the *bc* plane with two hole pockets bent at opposite directions. This gives rise to the behavior in Fig. 6(d). F_β also shows quasi-2D angle dependence with field rotated in *ab* plane with $\phi \leq 30^o$, however, with further increase the angle, F_β decreases quickly to 856 T at $\phi = 90^o$ (H//*a*). This can be explained by the bow-tie-like electron pocket, when $\phi \leq 30^o$; quantum oscillations are due to the the orbit crossing all the pocket, flat side wall gives rise to quasi-2D behavior. When $\phi > 30^o$ quantum oscillations are due to the orbit on the neck of the bow tie, which decreases quickly with angle and show minimum value with $\phi = 90^o$ (H//*a*), even smaller than hole pocket.[10,14] The Fermi surface measured by dHvA agrees well with the theoretical calculation, giving indirect support for the band structure and predicted type-II Weyl points.[10]

In addition to charge compensation, spin-orbital coupling and the related spin and orbital angular momentum texture also play an important role in large MR in WTe_2.[31] The spin textures can reduce the resistivity by suppressing the backscattering channel of the quasiparticles, and large MR is observed when the external magnetic field changes the spin structure and lifts the scattering protection. The carrier density in WP_2 is relatively high,[15,17] and the spin texture might be important for the large MR in WP_2. Moreover, WP_2 crystal structure lacks weakly Van der Waals bonded layers, yet still features Fermi surface with 2D angular dependence of MR. This might be attributed to the spin textures, which show large anisotropy.[31] Assuming the circular cross section of the hole Fermi pockets, the spin-orbital coupling induced band splitting in MoP_2 is estimated to be $k_{\alpha'}$ - $k_\alpha = 6.0 \times 10^{-3}$ Å^{-1}, similar to that in MoP and smaller than 3.2×10^{-2} Å^{-1} in WP_2.[17,32] As a result, the different values of MR and the angular dependence of MR can be explained by the strength of spin-orbital coupling. Our measurements indicate that strong spin-orbital coupling plays an important role in the transport properties of MoP_2, which requires additional studies.

IV. CONCLUSIONS

In conclusion, our MR studies are consistent with the presence of both Dirac states and parabolic band with enhanced quasiparticle mass in MoP_2. The dHvA measurements reveal quasi-2D multiband transport and are in agreement with the calculated Fermi surface. Strong spin-orbital coupling is rather important in the electronic transport of MoP_2.

ACKNOWLEDGEMENTS

We thank David Szalda for help with Bruker APEXII measurements and John Warren for his help with SEM measurements. Work at BNL was supported by the U.S. DOE-BES, Division of Materials Science and Engineering, under Contract No. DE-SC0012704. Work at the

National High Magnetic Field Laboratory is supported by the NSF Cooperative Agreement No. DMR-1157490, and by the state of Florida.

[1] H. Weng, C. Fang, Z. Fang, B. A. Bernevig, and X. Dai, Phys. Rev. X **5**, 011029 (2015).

[2] X. Huang, L. Zhao, Y. Long, P. Wang, D. Chen, Z. Yang, H. Liang, M. Xue, H. Weng, Z. Fang, X. Dai, and G. Chen, Phys. Rev. X **5**, 031023 (2015).

[3] S. Y. Xu, I. Belopolski, N. Alidoust, M. Neupane, G. Bian, C. L. Zhang, R. Sankar, G. Q. Chang, Z. J. Yuan, C. C. Lee, S. M. Huang, H. Zheng, J. Ma, D. S. Sanchez, B. K. Wang, A. Bansil, F. C. Chou, P. P. Shibayev, H. Lin, S. Jia, and M. Z. Hasan, Science **349**, 613 (2015).

[4] A. A. Soluyanov, D. Gresch, Z. Wang, Q. Wu. M. Troyer, X. Dai, and B. A. Bernevig, Nature **527**, 495 (2015).

[5] Y. Xu, F. Zhang, and C. Zhang, Phys. Rev. Lett. **115**, 265304 (2015).

[6] A. A. Zyuzin, R. P. Tiwari, JETP Lett. **103**, 717 (2016).

[7] T. E. O'Brien, M. Diez, C. W. J. Beenakker, Phys. Rev. Lett. **116**, 236401 (2016).

[8] Zhijun Wang, Dominik Gresch, Alexey A. Soluyanov, Weiwei Xie, S. Kushwaha, Xi Dai, Matthias Troyer, Robert J. Cava, and B. A. Bernevig, Phys. Rev. Lett. **117**, 056805 (2016).

[9] B. Yan and C. Felser, Annual Review of Condensed Matter Physics **8**, 337 (2017).

[10] G. Autes, D. Gresch, M. Troyer, A. A. Soluyanov, and O. V. Yazyev, Phys. Rev. Lett. **117**, 066402 (2016).

[11] P. Blaha *et al.*, Comput. Phys. Commun. **147**, 71 (2002).

[12] J. P. Perdew, K. Burke, and M. Ernzerhof, Phys. Rev. Lett. **77**, 3865 (1996).

[13] S. Rundqvist and T. Lundstrom, Acta Chem. Scand. **17**, 37 (1963).

[14] N. Kumar, Y. Sun, K. Manna, V. Süss, I. Leermakers, O. Young, T. Förster, M. Schmidt, B. Yan, U. Zeitler, C. Felser, C. Shekhar, arXiv: 1703.04527

[15] R. Schönemann, N. Aryal, Q. Zhou, Y. -C. Chiu, K. -W. Chen, T. J. Martin, G. T. McCandless, J. Y. Chan, E. Manousakis, and L. Balicas, arXiv: 1706.10135.

[16] M. Ziman, *Electrons and Phonons* (Clarendon Press, Oxford, 1962).

[17] Aifeng Wang, D. Graf, Yu Liu, Qianheng Du, Jiabao Zheng, Hechang Lei, and C. Petrovic, Phys. Rev. B **96**, 121107(R) (2017).

[18] D. Chen, L. X. Zhao, J. B. He, H. Liang, S. Zhang, C. H. Li, L. Shan, S. C. Wang, Z. A. Ren, C. Ren, and G. F. Chen, Phys. Rev. B **94**, 174411 (2016).

[19] M. N. Ali, J. Xiong, S. Flynn, J. Tao, Q. D. Gibson, L. M. Schoop, T. Liang, N. Haldolaarachchige, M. Hirschberger, N. P. Ong, R. J. Cava, Nature **514**, 205 (2014).

[20] F. F. Tafti, Q. D. Gibson, S. K. Kushwaha, N. Haldolaarachchige, and R. J. Cava, Nature Phys. **12**, 272 (2015).

[21] A. B. Pippard, *Magnetoresistance in metals* (Cambridge University Press, Cambridge, 1989)

[22] M. L. Snodgrass, F. J. Blatt, Jon L. Opsal, and C. K. Chiang, Phys. Rev. B **13**, 574 (1976).

[23] J. E. Huffman, M. L. Snodgrass, and F. J. Blatt, Phys. Rev. B **23**, 483 (1981).

[24] R. J. Schwartz and F. Stangler, Phys. Status Solidi B **60**, K69 (1973).

[25] Y. Kopelevich, J. H. S. Torres, R. R. da Silva, F. Mrowka, H. Kempa, and P. Esquinazi, Phys. Rev. Lett. **90**, 156402 (2003).

[26] Kefeng Wang, D. Graf, Hechang Lei, S. W. Tozer, and C. Petrovic, Phys. Rev. B **84**, 220401 (2011).

[27] H. -H. Kuo, J. H. Chu, S. C. Riggs, L. Yu, P. L. McMahon, K. De Greve, Y. Yamamoto, J. G. Analytis, and I. R. Fisher, Phys. Rev. B **84**, 054540 (2011).

[28] K. K. Huynh, Y. Tanabe, and K. Tanigaki, Phys. Rev. Lett. **106**, 217004 (2011).

[29] D. Shoeneberg, *Magnetic Oscillation in Metals* (Cambridge University Press, Cambridge, 1984).

[30] B. Q. Lv, Z.-L. Feng, Q.-N. Xu, X. Gao, J.-Z. Ma, L.-Y. Kong, P. Richard, Y.-B. Huang, V. N. Strocov, C. Fang, H.-M. Weng, Y.-G. Shi, T. Qian and H. Ding, Nature **546**, 627 (2017).

[31] J. Jiang, F. Tang, X. C. Pan, H. M. Liu, X. H. Niu, Y. X. Wang, D. F. Xu, H. F. Yang, B. P. Xie, F. Q. Song, P. Dudin, T. K. Kim, M. Hoesch, P. K. Das, I. Vobornik, X. G. Wan, and D. L. Feng, Phys. Rev. Lett. **115**, 166601 (2015).

[32] C. Shekhar, Y. Sun, N. Kumar, M. Nicklas, K. Manna, V. Süβ, O. Young, I. Leermakers, T. Förster, M. Schmidt, L. Muechler, P. Werner, W. Schnelle, U. Zeitler, B. Yan, S. S. P. Parkin, C. Felser, arXiv: 1703.03736.